aerospace

MDPI

Article

Parametric Study on Counterflowing Jet Aerodynamics of Apollo Re-Entry Capsule

Zhi-Kan Liu [1,2], Yi-Lun Liu [1,2], Shen-Shen Liu [3] and Long-Fei Li [3,*]

[1] School of Aeronautics, Northwestern Polytechnical University, Xi'an 710072, China; liuzhikan@mail.nwpu.edu.cn (Z.-K.L.); 2023260284@mail.nwpu.edu.cn (Y.-L.L.)
[2] National Key Laboratory of Aircraft Configuration Design, Xi'an 710072, China
[3] Computational Aerodynamics Institute, China Aerodynamics Research & Development Center, Mianyang 621000, China; lsssml1990@126.com
* Correspondence: lf_li@nuaa.edu.cn

Abstract

As an active flow-control technology, the counterflowing jet can reduce drag by reconstructing the flow field structure during the re-entry of a vehicle, thereby mitigating the adverse effects of high overload on personnel. However, variations in the angle of attack (AoA) and nozzle mass flow rate tend to induce transitions in its flow field modes and fluctuations in drag reduction performance. To further investigate the aerodynamic interference characteristics of the counterflowing jet during the re-entry process, this study focused on a 2.6% subscale model of the Apollo return capsule. The Reynolds-averaged Navier–Stokes (RANS) equations turbulence model was employed to numerically analyze the effects of different mass flow rates and freestream AoAs on the flow field modes and the drag behavior. The results indicate that with an increase in AoA, the flow field structure of the long penetration mode (LPM) is likely to be destroyed, and the shock wave shape exhibits significant asymmetric distortion. In contrast, the flow field structure of the short penetration mode (SPM) remains relatively stable; however, the bow shock and Mach disk exhibit two typical offset patterns, whose offset characteristics are jointly regulated by the mass flow rate and AoA. In terms of drag characteristics, the AoA significantly weakens the drag reduction effect of the LPM. In contrast, the SPM can maintain a stable drag reduction efficiency of approximately 50% within a certain AoA range. Nevertheless, as the AoA further increases, the drag reduction effect of the SPM gradually diminishes.

Keywords: counterflowing jet; apollo return capsule; short penetration mode; drag reduction

Check for updates

Academic Editor: Kyun Ho Lee

Received: 25 November 2025
Revised: 17 December 2025
Accepted: 18 December 2025
Published: 22 December 2025

Copyright: © 2025 by the authors. Licensee MDPI, Basel, Switzerland. This article is an open access article distributed under the terms and conditions of the Creative Commons Attribution (CC BY) license.

1. Introduction

Atmospheric re-entry exposes spacecraft to extreme hypersonic flow conditions, typically at Mach numbers exceeding 30 [1], under which strong bow shocks form ahead of the vehicle [2]. These conditions result in substantial aerodynamic drag and severe aerodynamic load levels [3,4]. Excessive loads during re-entry have been shown to compromise flight safety, making the achievement of stable and controllable drag reduction a critical requirement for hypersonic re-entry vehicles [5]. Among various flow-control strategies, counterflowing jets have attracted sustained attention due to their capability to actively modify the flow field upstream of the vehicle [6–9].

Counterflowing jets in blunt-body return capsule configurations induce a forebody recirculation region and increase the bow shock stand-off distance under hypersonic re-entry conditions, thereby restructuring the forebody flow field [10–13]. The interaction between

the counterflowing jet and the incoming flow generally exhibits two characteristic regimes, namely the long penetration mode (LPM) and the short penetration mode (SPM) [14,15]. These regimes differ markedly in terms of recirculation zone size, shock stand-off distance, and flow field stability [16]. Previous studies have shown that increasing the jet pressure ratio can promote a transition from LPM to SPM, thereby enhancing flow stability; however, this transition is accompanied by a substantial increase in jet mass flow rate [17]. As a result, variations in jet operating conditions directly influence the forebody pressure distribution, aerodynamic loads, and overall drag of the return capsule. Under appropriately selected jet conditions, counterflowing jets can achieve significant drag reduction compared with the no-jet configuration [18,19]. Numerical and experimental studies based on scaled Apollo return capsule models further indicate that counterflowing jets are effective in reducing forebody pressure and thermal loads [20,21], and the associated drag reduction contributes to mitigating re-entry overload levels [22,23].

Most existing studies have focused on counterflowing jet behavior under zero angle-of-attack conditions [16,24,25]. In practical re-entry trajectories, however, return capsules typically operate at non-zero angles of attack while the jet mass flow rate varies. Under such conditions, counterflowing jet-induced flow structure evolution can substantially modify the recirculation zone extent, shock position, and aerodynamic load distribution. Despite this, a systematic and quantitative characterization of the coupling between flow structure variations and aerodynamic responses across different angles of attack and jet mass flow rates remains unavailable. In the absence of such quantitative correlations, assessments of drag reduction performance based solely on individual flow structure features or drag metrics are insufficient to capture the overall aerodynamic response and may lead to biased evaluations of counterflowing jet effectiveness, thereby increasing uncertainty in re-entry aerodynamic design.

Based on these considerations, the present study performs numerical simulations of a 2.6% scaled Apollo return capsule model to investigate counterflowing jet effects under re-entry-relevant conditions. Geometric parameters are introduced to quantitatively describe the evolution of jet-induced flow structures, and the variation in flow topology is systematically analyzed over a range of angles of attack and jet mass flow rates. Furthermore, the relationship between flow structure evolution and changes in aerodynamic loads and drag is examined. The objective of this study is to improve the physical understanding of counterflowing jet behavior under complex re-entry conditions and to provide a quantitative basis for the safe application and parameter optimization of counterflowing jet technology in return capsule re-entry.

2. Numerical Methodology

2.1. Baseline Solver

All cases in the present work are solved by a hybrid-unstructured–mesh-based three-dimensional Navier–Stokes solver FlowStar [26]. The FlowStar V2.0 is a computational fluid dynamics (CFD) software developed by the China Aerodynamics Research and Development Center. It demonstrates high accuracy and good adaptability in simulating complex flow problems and can be effectively applied in a number of research areas, including aerodynamic performance analysis of high-lift configurations, study of Reynolds number effects [27], and aerodynamic analysis of unsteady dynamic deformation structures [28]. Based on its unstructured grid and cell-centered finite-volume numerical framework, and incorporating advanced algorithms such as the improved HLLE++ scheme [29] and viscous boundary-layer mesh adaptation [30], the FlowStar shows excellent convergence stability and computational accuracy in simulating complex flow phenomena.

The numerical simulations implemented in FlowStar are based on the governing framework of the three-dimensional compressible Reynolds-averaged Navier–Stokes (RANS) equations. The equations are expressed in integral form, as provided by Equation (1):

$$\frac{\partial}{\partial t}\iiint_{\Omega} \boldsymbol{Q}dV + \iint_{\partial\Omega} \boldsymbol{F}(\boldsymbol{Q})\cdot\boldsymbol{n}dS = \iint_{\partial\Omega} \boldsymbol{G}(\boldsymbol{Q})\cdot\boldsymbol{n}dS \quad (1)$$

where the vector of conservative variables, $\boldsymbol{Q}$, is defined as $\boldsymbol{Q} = [\boldsymbol{\rho}\ \boldsymbol{\rho u}\ \boldsymbol{\rho v}\ \boldsymbol{\rho w}\ \boldsymbol{\rho E}]^{\boldsymbol{T}}$. Here, $\boldsymbol{\rho}$ is the fluid density; $\boldsymbol{u}$, $\boldsymbol{v}$, and $\boldsymbol{w}$ are the components of the flow velocity in the $\boldsymbol{x}$, $\boldsymbol{y}$, and $\boldsymbol{z}$ directions, respectively; and $\boldsymbol{E}$ is the total energy per unit mass. $\mathbf{F}(\mathbf{Q})$ is the vector of convective fluxes, and $\mathbf{G}(\mathbf{Q})$ is the vector of viscous fluxes.

In terms of the turbulence model, the shear stress transport (SST) model is selected in this paper. The model combines two widely used two-equation turbulence models, the k-ε model and the k-ω model, through a mixing function F1. This combination allows the excellent near-wall properties of the k-ω model to be combined with the insensitivity of the k-ε model to the freestream parameters. As an eddy viscosity model, the Menter SST method also requires the modelling of Reynolds stresses using the Boussinesq simulation equation. The closure of the model is accomplished by solving the two transport equations for turbulent kinetic energy $\widetilde{k}$ and specific dissipation rate ω simultaneously. The details of the terms and constants about the SST turbulence model can be found in Ref. [31].

2.2. Computational Setup

The flow field is solved using a Reynolds-averaged Navier–Stokes (RANS) approach with the SST turbulence model. A cell-centered finite volume method is employed for spatial discretization to ensure conservation and accuracy. The convective fluxes are computed using a second-order upwind Roe scheme, while the viscous fluxes are evaluated with a second-order central difference scheme. Second-order spatial accuracy is achieved through Barth's interpolation method, and gradients are calculated using the Green–Gauss formulation. For steady simulations, the data-parallel lower-upper relaxation (DPLUR) method is adopted, whereas unsteady simulations are conducted using a second-order fully implicit dual-time stepping scheme.

3. Geometric Configuration and Validation

3.1. Model Geometry

The geometric model presented in this paper is based on the 2.6% subscale model of the Apollo capsule with a central nozzle, which produces exit Mach numbers of Ma_j = 2.94. The related geometric parameters are provided in Figure 1a, and the model is provided in Figure 1b. The wind tunnel experiments were executed by Daso et al. [20] in the Transonic Wind Tunnel at NASA's Marshall Space Flight Center. The nozzles were run at a series of design flow rates (0.00, 0.0227, 0.0454, 0.1134, 0.1588, and 0.2268 kg/s) [20]. The composition of both the free and jet streams was air ($\gamma_\infty = \gamma_j$ = 1.4). Pressure and air temperature data were collected from 56 hydrostatic ports and 15 heat flux sensors on the model, but the quality of the pressure data was deemed insufficient for post-test comparison [32]. Therefore, the findings of the CFD numerical simulations are subsequently evaluated in comparison with the experimental schlieren images and the axial location of the detached bow shock.

3.2. Computational Mesh

As shown in Figure 2a, the configuration of the model is a 2.6% subscale Apollo capsule with a central nozzle and a support sting. The computational mesh of the model is shown in Figure 2b, which is generated using a structural mesh. The nonreflecting pressure

far field is used for the outer boundary condition. The inner boundary adopts a viscous wall boundary condition. The first layer spacing of the boundary layer corresponds to Y+ < = 1, and the normal height growth rate is obtained as 1.15. The mesh employed for all the other computations, which involves the presence of a nozzle, contains approximately 12.77 million cells.

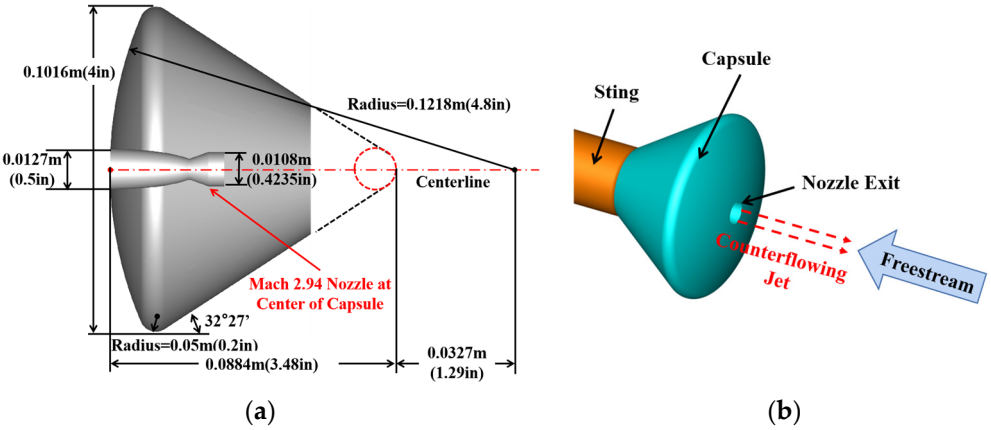


Figure 1. Geometry of the Apollo capsule model (2.6% scale). (**a**) Schematic sketch defining key dimensions: the conical head (top diameter: 0.1016 m), the connecting shoulder (radius: 0.05 m), and the centerline nozzle. (**b**) Three-dimensional solid model, illustrating the capsule body, support sting, and the orientation of the counterflowing jet relative to the freestream direction.

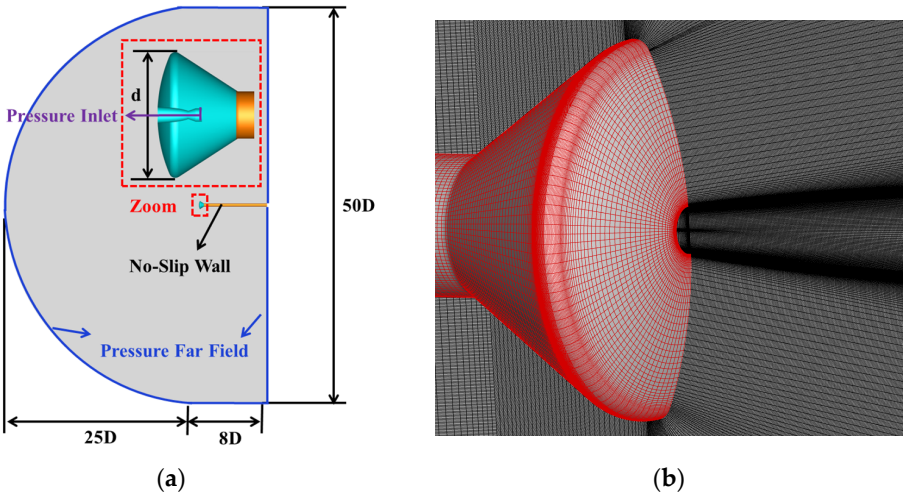


Figure 2. Diagram of computational mesh. (**a**) Source area for computation domain. (**b**) Computational mesh distribution details.

3.3. Computational Condition

In this paper, the central nozzle is run with a series of design mass flow rates (0.0227, 0.0453, 0.0681, 0.0815, 0.0907, 0.1134, 0.1589, 0.2268, and 0.4536 kg/s). The corresponding nozzle stagnation pressures and temperatures for these cases are provided in Table 1 The purpose is to validate by comparing with the results of the wind tunnel experiments Daso et al. [20] performed and further investigate the influence of mass flow rate. At the same time, most studies on the re-entry of Apollo capsules note that the normal re-entry angle is controlled within a narrow range of 5.5–7.5°. However, during the atmospheric re-entry phase of the Apollo 4 mission, the command module achieved a maximum angle of attack of 24.4° [33]. To explore the underlying laws and address extreme conditions in engineering practice, a series of freestream angles of attack (0°, 5°, 10°, 20°, 25°) are further evaluated in the following sections.

Table 1. Freestream and counterflowing nozzle jet conditions simulated in the present study.

Freestream Conditions					
M_∞	P_0 (atm)	P (atm)	T_0 (K)	T (K)	Re_∞, 1/d
3.48	3.061	0.04129	333.33	97.406	1.63×10^6
Counterflowing nozzle jet conditions					
Case ID		$\dot{m}_j$ (kg/s)	P_0 (atm)	P (atm)	T_0 (K)	T (K)
Baseline						
1		0.0227	3.0340	2.9526		
2		0.0453	6.0680	5.9052		
3		0.0681	9.1020	8.8578		
4		0.0815	10.9224	10.6294		
5		0.0907	12.1360	11.8104	300.00	297.68
6		0.1134	15.1701	14.7630		
7		0.1589	21.2381	20.6682		
8		0.2268	30.3402	29.5261		
9		0.4536	60.6803	59.0521		

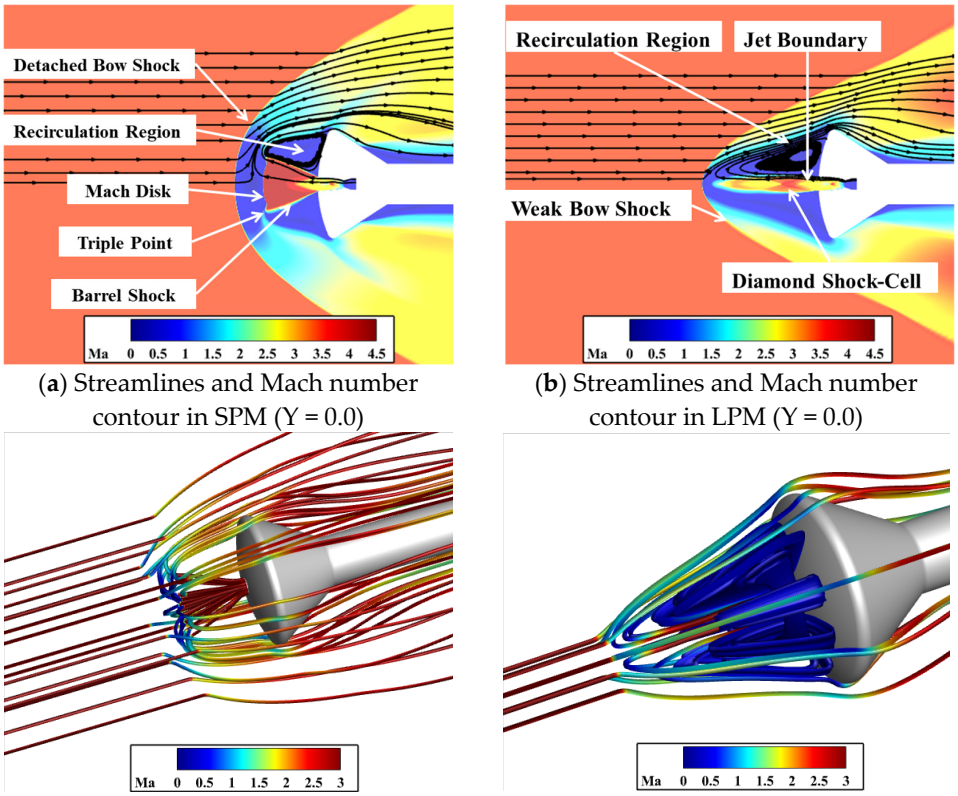
Table 1 lists the following variables: P_0 and P are stagnation and static pressure, respectively; T_0 and T are stagnation and static temperature, respectively; $\dot{m}_j$ is the mass flow rate of the nozzle; and Re_∞ is the freestream Reynolds number.

3.4. Validation of Numerical Results and Characterization of Flow Field

Previous studies have demonstrated that when the LPM occurs in a supersonic freestream, the ratio of the nozzle exit area to the fuselage reflective surface area typically needs to be approximately 1:15 [9,32]. In the present study, the area ratio of the designed model is set to 1:63, which allows for the reproducibility of both the SPM and LPM under varying mass flow rate conditions.

Figure 3a,b show the flow structure characterization for the jet issuing from the central nozzle against the supersonic freestream, the former is the SPM and the latter is the LPM. The SPM should give rise to a symmetric jet structure defined along a constant pressure boundary, with a barrel shock and a terminal Mach disk under highly under-expanded conditions. In the subsonic region between the detached bow shock and the Mach disk, a stagnation point should be formed on the contact surface along the direction of the body axis. And for the LPM, the jet is composed of a series of incident and reflected oblique shock waves which provide the conventional diamond shape. The total pressure of the jet gradually decreases as it passes through this shock system, ending in a weaker shock, after which the jet flow becomes subsonic [3]. Mach streamlines are connected circumferentially in Figure 3c,d, which can reflect the three-dimensional draining effect of the flow in the recirculation region. With an increase in the jet mass flow rate leading to a disruption of the aero-acoustic feedback loop [34,35], the collapse of the subsonic velocity region is the physical trigger that leads to the observed collapse of the fast flow field and the mode transition from a unsteady LPM to a steady SPM [9].

Schlieren images are compared with the density gradient contours in Figure 4 (no original experiment data available for 0.0681, 0.0815, 0.0907, and 0.4536 kg/s mass flow rates). When the counterflowing jet is an LPM, the results are for reference only due to the unsteady nature of the LPM. As the mass flow rate increases, the counterflowing jet changes to the SPM, the predicted distance of the detached bow shock agrees very well with the experimental data. More importantly, interference between the Mach disk and the barrel shock leads to bending of the ends of the Mach disk, and the bent Mach disk also interferes with the free shear layer.



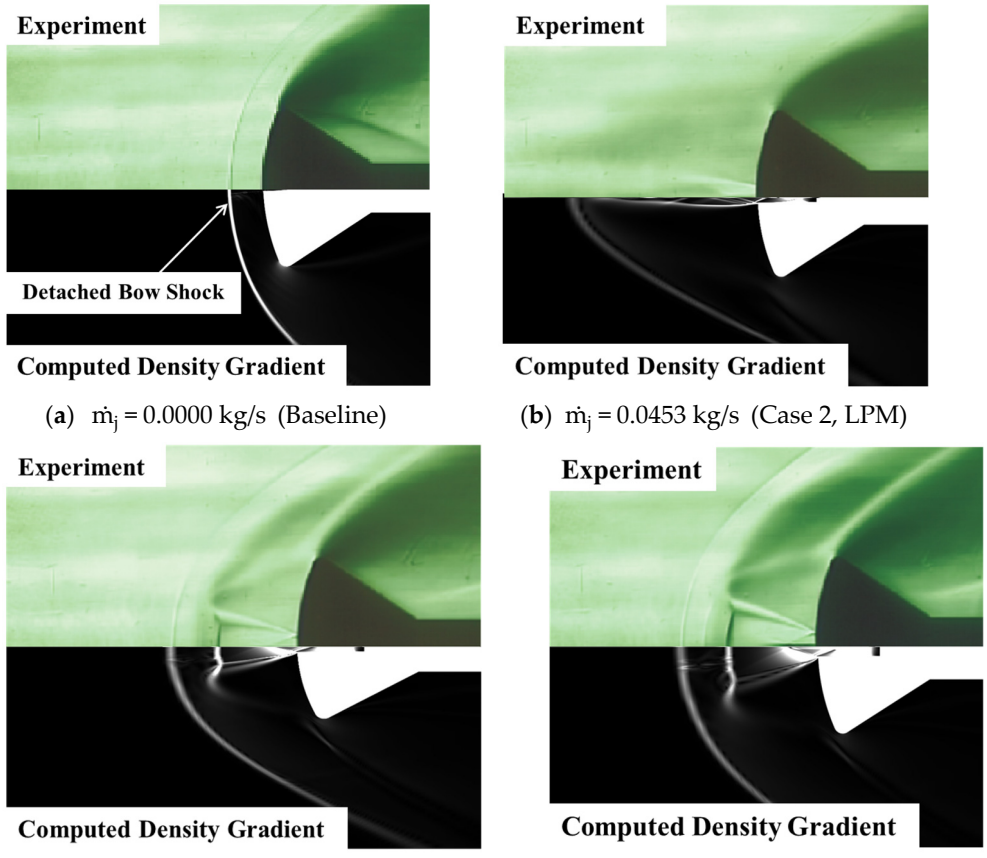
(**a**) Streamlines and Mach number contour in SPM (Y = 0.0)

(**b**) Streamlines and Mach number contour in LPM (Y = 0.0)

(**c**) Mach streamlines in SPM

(**d**) Mach streamlines in LPM

Figure 3. Streamlines and Mach number contours for SPM (Case 8) and LPM (Case 2) (α = 0°).



(**a**) $\dot{m}_j$ = 0.0000 kg/s (Baseline)

(**b**) $\dot{m}_j$ = 0.0453 kg/s (Case 2, LPM)

(**c**) $\dot{m}_j$ = 0.1589 kg/s (Case 7, SPM)

(**d**) $\dot{m}_j$ = 0.2268 kg/s (Case 8, SPM)

Figure 4. Computed density gradient versus experimental schlieren image (α = 0°).

A grid independence study was also conducted for the no-jet case (Baseline). Three grids with different resolutions were used: a coarse grid (Grid 1, 5.31 million cells), a medium grid (Grid 2, 12.77 million cells), and a fine grid (Grid 3, 20.12 million cells). The results of the medium grid matched very closely with the refined grid pressure plots as shown in Figure 5a. Consequently, the medium grid was selected for further analysis due to its balance between computational efficiency and accuracy. In Figure 5, ΔS refers to the distance from a point on the capsule surface to the nozzle centerline, normalized using R. And ΔX is the distance from a point on the nozzle centerline to the nozzle exit, dimensionless using D. R and D are the radius and diameter of the maximum cross-sectional area of the capsule, respectively.

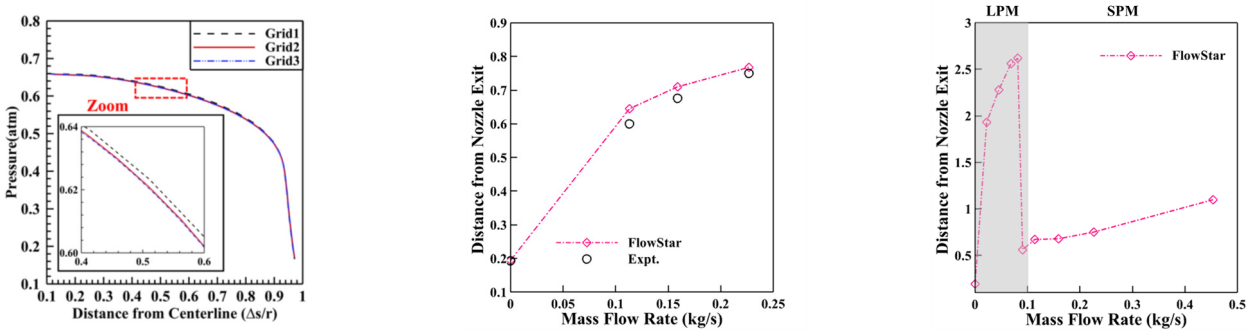


Figure 5. Grid independence study and axial location of flow feature (α = 0°). (**a**) Grid independence study of no-jet case. (**b**) Comparison of bow shock and stand-off distances; (**c**) shock stand-off distance in all cases.

Figure 5b compares the predicted and experimental shock stand-off distance. As the total jet pressure increases, the degree of under-expansion of the jet increases, and the flow structure becomes more steady and more stable [35]. Therefore, the predicted distance of the detached bow shock gradually gets closer to the experimental data [20].

Figure 5c summarizes the shock stand-off distance against the mass flow rate across all cases. The results show that under the LPM, the shock stand-off distance extends progressively forward as the mass flow rate increases, reaches a maximum, and retreats significantly before converting to the SPM; then, the distance continues to increase in this mode. In addition, it can be observed that the mass flow rate for jet mode conversion is approximately 0.0907 kg/s.

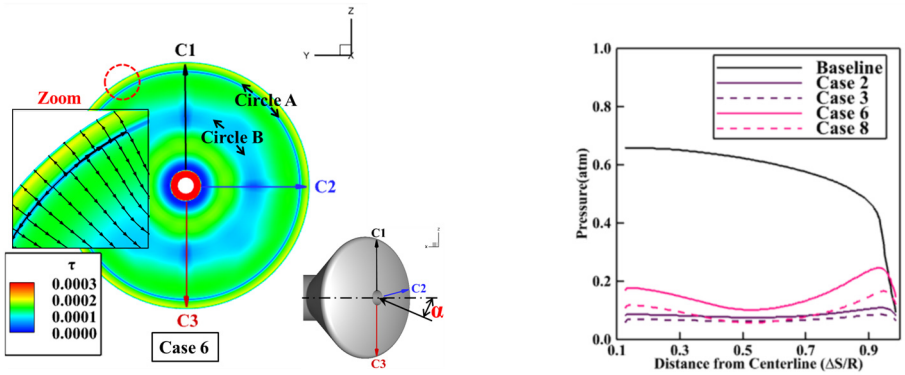
4. Results and Discussion

The influence of various nozzle mass flow rates and freestream angles of attack on the flow field structure around the capsule, including key features such as the reattachment point location, Mach disk, and bow shock, is examined. Furthermore, the aerodynamic loads on the capsule, particularly the drag characteristics, are thoroughly investigated in relation to the evolving flow structures. The analysis reveals the transition characteristics between jet penetration modes (LPM and SPM), the deformation mechanisms of the flow field under angled attack, and the underlying correlation between these flow features and the resultant drag reduction performance.

4.1. Baseline Flow Structure of the Counterflowing Jet

The recirculation zone is a key feature of the counterflowing jet flow, with the location of the reattachment point and the pressure serving as its primary parameters [36]. In order to further study the reattachment of flow, the reattachment point of different mass flows under a 0° angle of attack is analyzed. As illustrated in Figure 6a, the pressure distributions

of different circumferential positions on the surface of the return capsule are extracted at positions C1, C2, and C3. It can be observed that there are two locations on the object surface where the friction approaches zero: one at Circle A located near the outer edge and the other at Circle B. The former phenomenon is due to the flow separation caused by the recirculation zone, which leads to the formation of a reattachment line and the maximum value in Figure 6b. The latter phenomenon can be attributed to the curvature of the windward side of the capsule, the approximate constant pressure within the recirculation region, and the closer distance between the recirculation region and the wall at Circle B. These factors contribute to an increase in velocity at Circle B and a subsequent decrease in pressure, which corresponds to the minimum value appearing in Figure 6b.



(**a**) Skin friction contours and streamlines (**b**) Pressure distribution in some cases

Figure 6. Circumferential pressure at capsule face with and without counterflowing jet ($\alpha = 0°$).

In addition, the shape of the recirculation region reflects the effect of the counterflowing jet on the capsule, altering its aerodynamic properties, as well as the structure of the nearby flow field. Combined with the small change in the position of the reattachment point described above, it can be found that the shape of the recirculation region is essentially dependent on the mass flow rate of the jet, i.e., the degree of expansion of the gas, for constant free flow parameters.

As shown by the numerical results under SPM conditions, the flow field structures exhibit a high degree of similarity across different mass flow rates. To facilitate a quantitative description of these observed structures, a set of geometric parameters is introduced to characterize the expansion state of the counterflowing jet and the shape of the recirculation region.

As shown in Figure 7, L_j is the length of Mach disk, L_d is the diameter of the nozzle exit, S_d is the distance from the nozzle exit to the maximum cross-section, S_j is the distance between the Mach disk and the nozzle exit, L_r is the length of recirculation region boundary in the direction of the vertical nozzle centerline, θ is the angle of the jet boundary, and β is the angle of the recirculation region lateral boundary. The jet boundary angle θ and recirculation region boundary angle β are defined, respectively, as:

$$\theta = arctan\left(\frac{L_j - L_d}{2 \cdot S_j}\right) \tag{2}$$

$$\beta = arctan\left(\frac{d - L_j - 2 \cdot L_r}{2 \cdot (S_j + S_d)}\right) \tag{3}$$

β, θ, and the length ratio S_j/L_d directly reflect the shape of the recirculation region and the expansion of the counterflowing jet under the SPM, as shown in Table 2. It is given that Case 5 is proximate to the point of transition in mode, with a significant alteration in the

position of the reattachment point being apparent. Consequently, this case is not deemed to be a suitable subject for consideration. It can be found that in the SPM, with the increase in mass flow rate, the length of the Mach disk increases, the jet boundary angle gradually increases, and the recirculation region boundary angle gradually decreases.

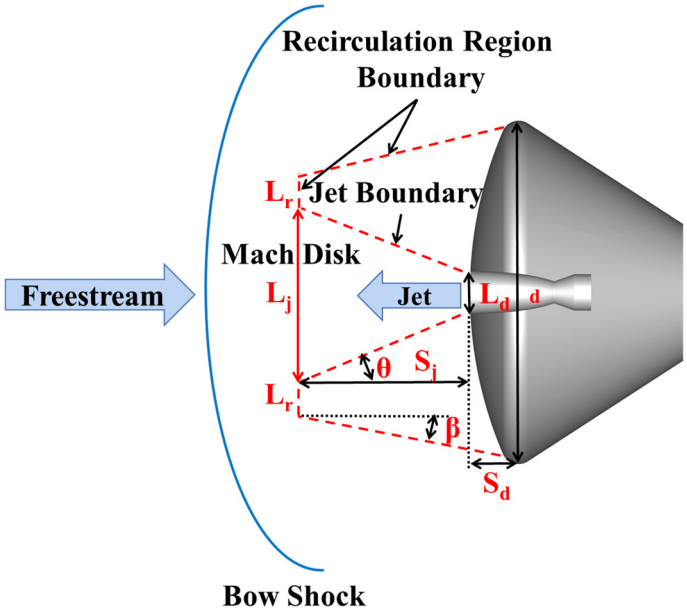


Figure 7. Schematic representation of counterflowing jet characterization parameters.

Table 2. Characterization parameters with different mass flow rates in SPM.

CaseID	L_j/L_d	L_r/L_d	S_j/L_d	tan(θ)	θ	tan(β)	β
6 (0.1134 kg/s)	2.3492	0.9465	3.2674	0.2065	11.6676°	0.2465	13.8473°
7 (0.1589 kg/s)	2.9756	0.8225	3.5605	0.2774	15.5040°	0.1770	10.0374°
8 (0.2268 kg/s)	3.9206	0.7753	3.7268	0.3918	21.3952°	0.1313	7.4801°
9 (0.4536 kg/s)	6.4048	0.7117	4.6752	0.5302	27.9325°	0.0298	1.7069°

4.2. Effect of Angle of Attack on Flow Structure Deformation

In addition to the 0° angle of attack, different nozzle mass flow rates at other angles are numerically simulated to investigate the effect of angle of attack on the flow structure. The results at partial mass flow rates are provided in Figure 8. The operating conditions were selected as Case 2 for the LPM and Cases 6 and 9 for the SPM. In both modes, the recirculation region is deformed, and the location of the reattachment point changes significantly. In Figure 8b, the destruction of LPM's diamond shock-cell structure is observed.

The following focuses on a specific analysis of the flow structure of the SPM, which is best understood in conjunction with Figure 8. At a 0° angle of attack, the curvature of the Mach disk is different due to the different mass flow rates. It defines the one along the jet flow direction as convex and the opposite as concave. For Case 7, the Mach disk is concave along the axial direction, while for Case 9, it is convex, as Figure 8 shows. The transition point for Mach disk curvature is roughly around a mass flow rate of 0.2268 kg/s. At a 10° angle of attack, its main structures, such as the recirculation region, Mach disk, and detached bow shock, are relatively stable. However, a certain degree of structural deformation is still observed. The following analysis will investigate the distinctions and causal factors underlying the two deformations of the flow structure in an in-depth manner.

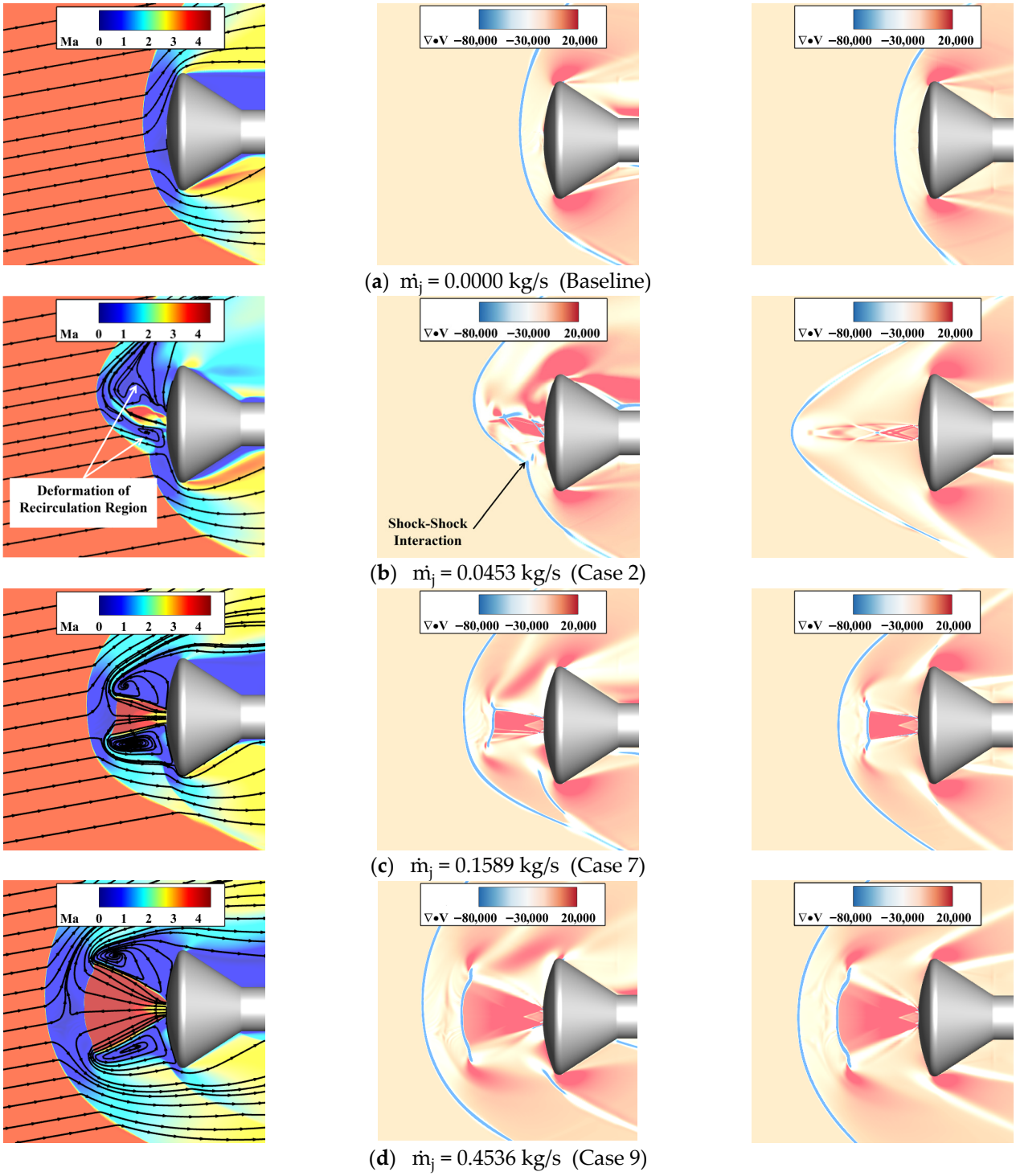


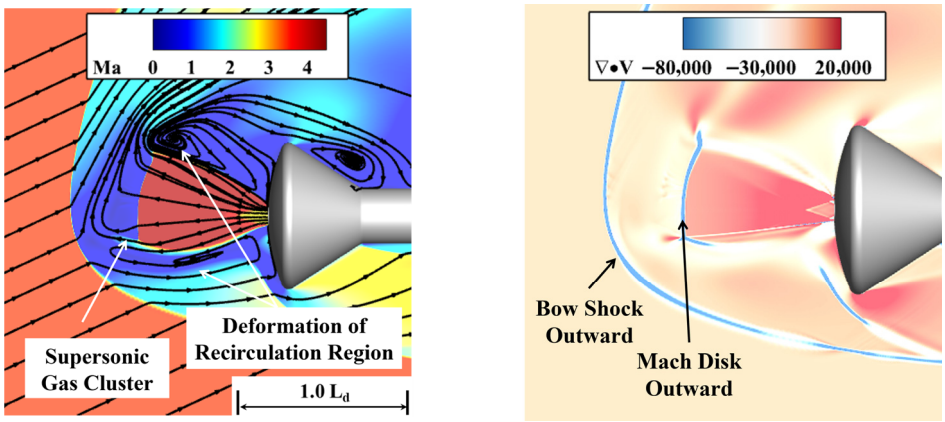
Figure 8. Mach number and velocity divergence contours (Y= 0.0, $\alpha = 10^\circ$ for the first two columns, and $\alpha = 0^\circ$ for the third column).

In terms of flow structure, the most obvious difference between Case 7 and Case 9 is the shape and size of the recirculation region. Firstly, it should be noted that in the following, the outer boundary of the recirculation region refers to the boundary on the side away from the nozzle centerline, which is provided as an illustration in Figure 8a. As shown in Figure 8c, the outer boundary of the recirculation region on the windward side is squeezed by the freestream with an angle of attack, becoming elongated in the direction of the nozzle centerline. In the contrary, on the leeward side, the recirculation region increases in the vertical nozzle axial direction and decreases slightly in size along the nozzle axial

direction, as it is squeezed by the freestream. The aforementioned factors result in the disappearance of barrel shock and the triple point on the windward side and outward of the Mach disk. Between the recirculation region and the detached bow shock, there is a supersonic gas cluster on each side of the nozzle centerline, which maintains the shape of the detached bow shock. And its speed is significantly higher than that of the gases passing through the Mach disk. Because of the change in the shape of the recirculation region, the position and direction of the supersonic gas cluster change, and the Mach disk is transformed into the shape of an oblique shock. Due to the outward offset of the supersonic gas cluster's position and the weak deceleration effect of the oblique shock, the high-velocity gas and the jet passing through the Mach disk on the windward side have more kinetic energy. They will continue to flow forward and impact the detached bow shock, forming an outward shock phenomenon on the windward side.

As a comparison, Figure 8d demonstrates another variation in the flow structure for the 10° angle of attack. As the jet boundary angle increases and the recirculation region boundary angle decreases, the Mach disk on the windward side is squeezed more by the freestream, resulting in the shortening of the recirculation region along the nozzle centerline. On the windward side, the Mach disk moves inward and changes into a stronger normal shock, causing the supersonic gas cluster to vanish. Therefore, the jet streams passing through the Mach disk have less kinetic energy, and the detached bow shock moves inward.

Due to the different mass flow rates, the Mach disk and the recirculation region deform in different ways. This phenomenon can be attributed to the combined influence of the freestream and counterflowing jet, which is specifically analyzed in the previous section. Moreover, for a fixed mass flow rate, it can be thought that the deformation of the flow structure is also related to the magnitude of the angle of attack of the freestream. In order to verify this idea, an additional comparison is made in Case 9 at 25° angle of attack. Comparing Figure 9 with Figure 8d, it can be found that the outward and inward of the Mach disk and bow shock are opposite in both. In conjunction with the analysis above, this phenomenon is attributed to the fact that the increased angle of attack leads to a greater squeeze of the outer boundary of the recirculation region. Figure 9 demonstrates that the size of the angle of attack is also indeed one of the influencing factors. Therefore, the deformation of the flow structure is contingent upon the location where it is subjected to more squeeze by the freestream.

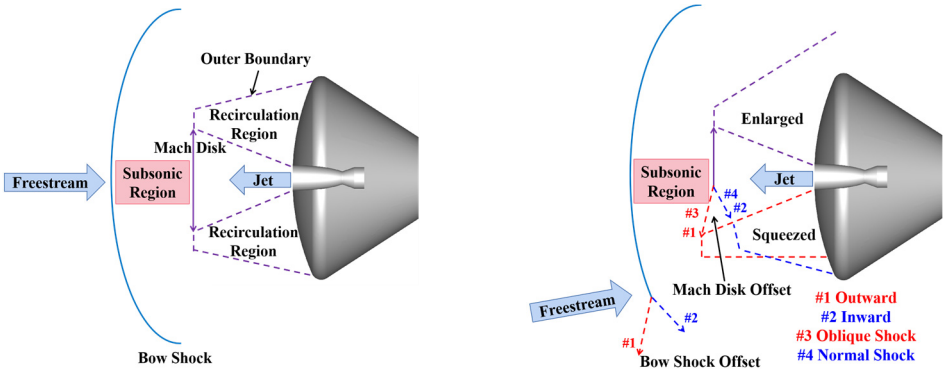


(**a**) Mach number contour (**b**) Velocity divergence contour

Figure 9. Mach number and velocity divergence contours for Case 9 (Y = 0.0, $\alpha = 25°$).

Combined with the above analysis, the deformation of the flow structure of the counterflowing jet under the SPM with the angle of attack is summarized in Figure 10. There are two types of inward and outward offsets of the detached bow shock and Mach

disk on the windward side. As demonstrated in Figure 10b, when the outer boundary of the recirculation region is squeezed, the Mach disk moves downstream of the jet into an oblique shock, and the detached bow shock moves outward. Conversely, when the Mach disk is squeezed more, the Mach disk is tilted upstream into a stronger normal shock, and the detached bow shock moves inward.



(**a**) 0° angle of attack (**b**) Finite angle of attack

Figure 10. Schematic representation of counterflowing jet structure in SPM.

Figure 11 provides the deformation of the flow structure under different working conditions in this paper. It can be divided into three types, which are the Mach disk and the detached bow shock's outward or inward offset and the destruction of the flow structure, respectively. The destruction of the flow structure can be understood as the windward recirculation region severely deforms, which essentially disappears. This phenomenon gives rise to the formation of a localized high-pressure zone on the capsule surface relative to the absence of jets. It can be seen that differences in the deformation of the flow structure are related to both the mass flow rate and the angle of attack. Each type has its own region of operating conditions.

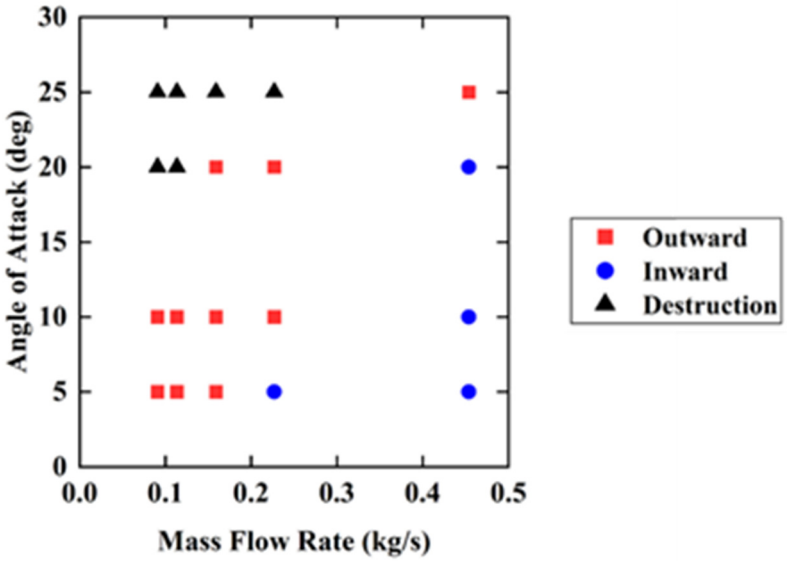
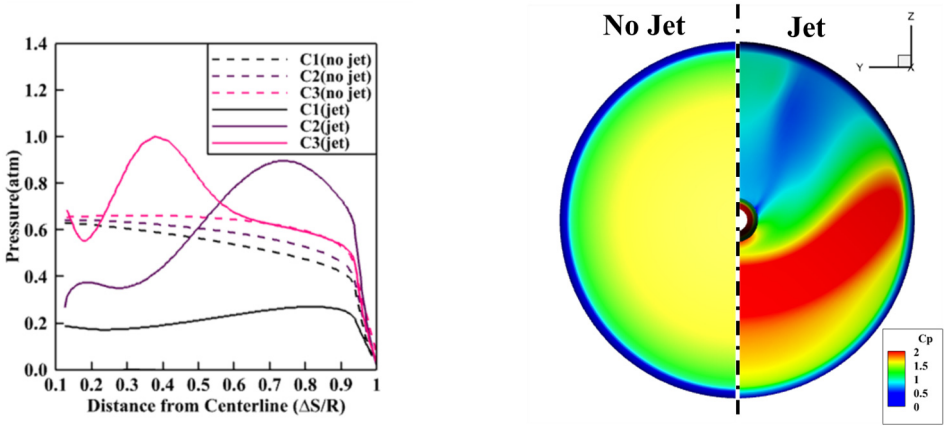


Figure 11. The deformation of the flow structure under different conditions.

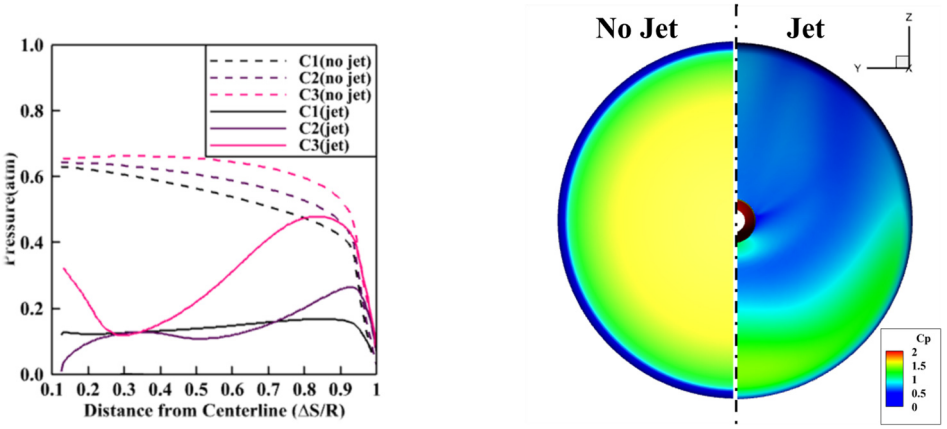
4.3. Impact on Drag Force

As illustrated in Figure 10b of the preceding section, at a 10° angle of attack, the structure of the LPM tends to be destroyed more readily, whereas the SPM still retains a relatively stable structure. To further demonstrate the effect of counterflowing jet on drag

at different angles of attack, pressure distribution at the capsule surface is first compared as plotted in Figure 12. When the 10° angle of attack occurs, on the windward side, the pressure is much higher with or without the counterflowing jet. It can be observed that the LPM exhibited a near-vanishing effect in Figure 12a. In some locations, the pressure from the reattachment flow is higher than the pressure without the jet. On the contrary, it can be found that the counterflowing jet under the SPM still reduces the pressure load considerably, as Figure 12b shows. Given the wide range of angles of attack that need to be investigated, drag in this section is limited to the SPM conditions.



(**a**) LPM (Case 2)



(**b**) SPM (Case 6)

Figure 12. Comparison of pressure distribution at capsule face, with and without counterflowing jet ($\alpha = 10^{\circ}$).

Counterflowing jet occurs in the outside of the jet low-pressure recirculation region; as a result, the surface pressure drops, and the capsule by the aerodynamic drag will be reduced. However, the jet reaction thrust can also contribute to the total drag. These two forces are in opposition to one another and thus require analysis and consideration together, specifically in regard to both aerodynamic drag and jet reaction thrust. Therefore, in varying operational settings, it is essential to select an optimal mass flow rate to achieve efficient drag reduction. The formulas for calculating the drag force on the capsule are shown below:

$$D_j = D_{out} + D_{in} + F_T \tag{4}$$

$$F_T = P_0 \cdot A \cdot cos\alpha \tag{5}$$

$$\Delta D = \frac{D_j - D_0}{D_0} \cdot 100\% \tag{6}$$

where D_j and D_0 are the total drag force with and without the jet, respectively; D_{out} is aerodynamic drag on the aircraft; D_{in} is drag force on the inner wall surface of the nozzle; F_T is the jet reaction thrust; P_{0j} is the total pressure at the nozzle inlet; S is the area of the nozzle inlet; α is the angle of attack; and ΔD is rate of change in drag force. The drag force in some of the jet conditions is compared with the results of Ref. [21] in Table 3.

Table 3. Comparison of computed drag with other Navier–Stokes code does not include sting.

	Case	Total Drag Force (N)	Total Drag Force (N) (UNIC Code [21])
$\alpha = 0°$	Baseline	433.2	434.4
	9 (0.4536 kg/s)	323.0	334.0
$\alpha = 10°$	Baseline	414.0	416.0
	9 (0.4536 kg/s)	329.7	326.0

As illustrated in Figure 11, only Case 9 is capable of maintaining structural stability at an angle of attack of 25°, so the drag force is not investigated for this angle-of-attack condition. Figure 13 provides the drag force, jet reaction thrust, and change in total drag force with and without the counterflowing jet at 0°, 5°, 10°, and 20° angles of attack. The best drag reduction is achieved by the counterflowing jet at a 0° angle of attack. The maximum drag reduction is 56.6%. When the angle of attack is within 10°, the total drag force change is maximum at a mass flow rate of 0.1134 kg/s. Jet reaction thrust increases with increasing mass flow rate. When it is greater than 0.1134 kg/s, the jet reaction thrust dominates total drag, with the increase in the jet reaction thrust exceeding the decrease in the aerodynamic drag.

The angle of attack creates an asymmetric effect in the flow field, which in turn affects the stability of the counterflowing jet flow structure and the drag reduction effect. From Figure 14, it can be found that as the freestream angle of attack increases, the drag reduction effect of the counterflowing jet gradually decreases. Combined with Figure 11, when the angle of attack is within 10°, the typical SPM's flow structure can be maintained, and the counterflowing jet still has a significant drag reduction effect in the SPM. Nevertheless, when the angle of attack reaches 20°, the drag reduction ability diminishes or even fails due to the deformation or destruction of the flow structure.

As can be seen from Figure 15, the degree of deformation in the recirculation region is markedly high, and the flow field is highly asymmetric when the angle of attack is 20°. Cases 5 and 6, with relatively small mass flow rates, have difficulty in maintaining the SPM's typical flow structure, which corresponds to the destruction in Figure 11. And it is accompanied by the emergence of a high-pressure region on the windward side of the capsule, which exhibits a pressure level that exceeds that observed in the absence of the counterflowing jet. This phenomenon is attributed to the fact that the freestream is congested by the counterflowing jet, as well as the capsule surface.

The pressure rises as the flow passes through the shock, and the location of the shock can be shown on the pressure contours. As shown in Figure 15, the detached bow shock and Mach disk on the windward side are outward in Cases 7 and 8, whereas they are oriented inward in Case 9. This is due to the increase in the mass flow rate; the position of the squeeze shifted from the outer boundary of the recirculation region to the Mach disk. Similarly, the three angles (10°, 20°, and 25°) of the state in Case 9 can also be compared with each other. As the angle of attack increases, the squeezed position changes from the Mach disk to the outer boundary of the recirculation region, and the detached bow shock and Mach disk are converted from an inward offset to an outward offset. These results further corroborate the credibility of the previously proposed explanation in this paper

regarding the formation mechanism underlying the existence of the two offsets in the SPM flow structure.

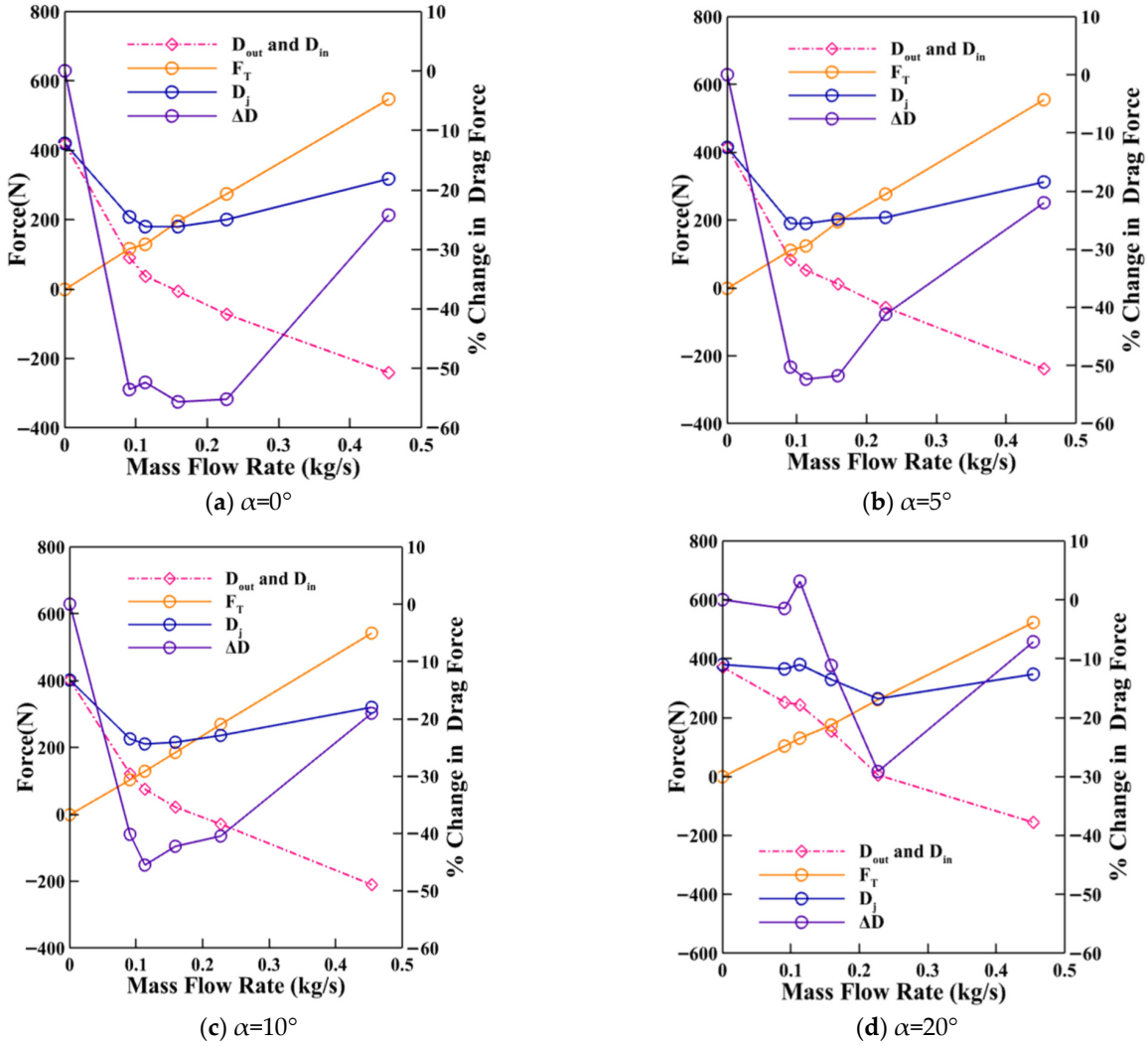


Figure 13. Drag force on capsule does not include sting for different angles of attack.

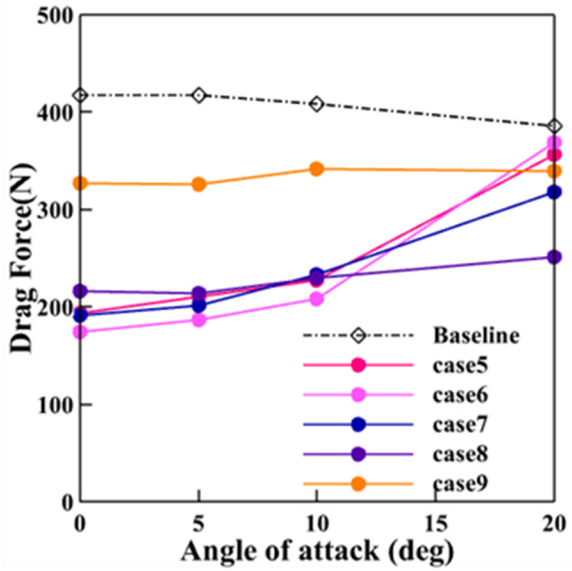


Figure 14. Variation in drag force with angle of attack for different mass flow rates.

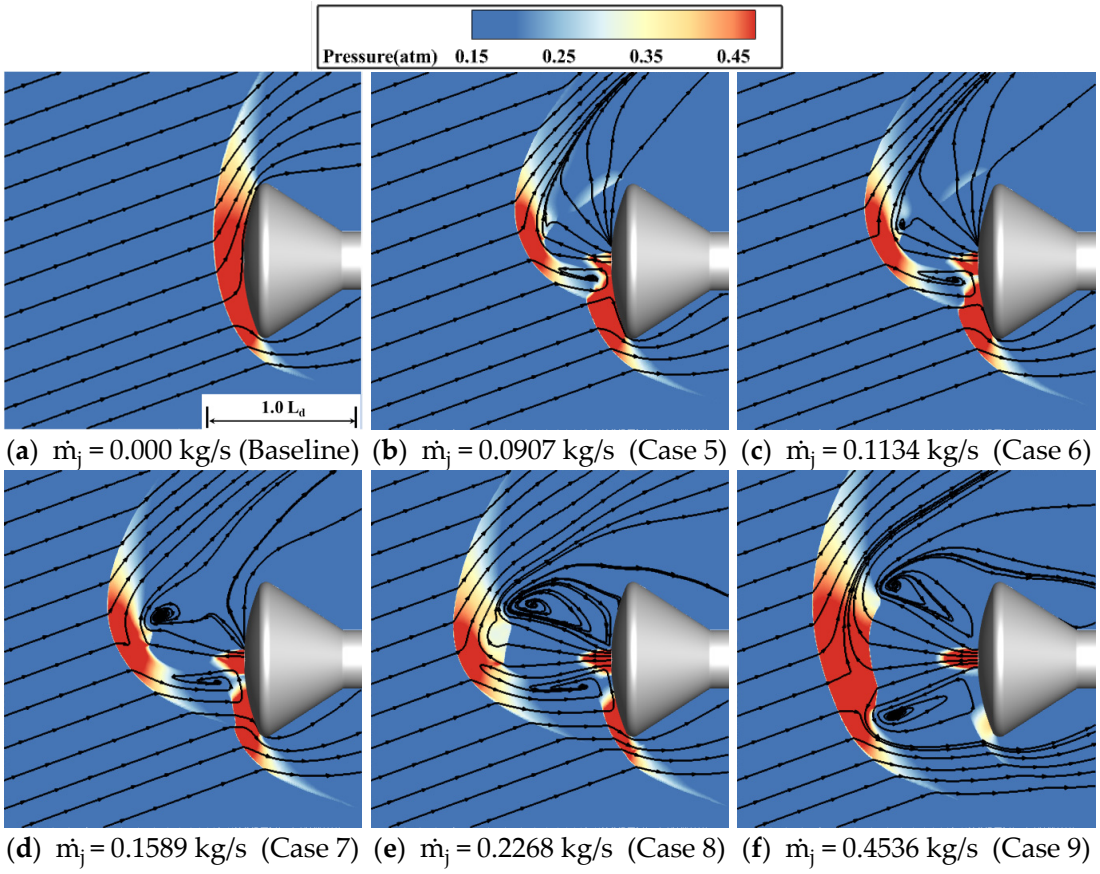


Figure 15. Pressure contours at the symmetry plane and surface of capsule (Y = 0.0, $\alpha = 20°$).

From an engineering perspective, when attempting to integrate the jet-based control system into an aircraft, the estimation of flow field reconstruction induced by the counterflowing jet and the drag reduction effect is of great significance during the conceptual design phase. Therefore, an attempt is made to summarize the research results of this paper by compiling the influence laws of mass flow rate and angle of attack, as presented in Table 4. Each item in this table corresponds to a specific combination of nozzle mass flow rate and freestream angle of attack, with the first row presenting structural variations and the second row showing drag reduction effects.

Table 4. Summary of parameter influences.

$\dot{m}_j$ \ α	0°	5°	10°	20°	Influence
<0.0907 kg/s	Highly unstable				High
0.0907 kg/s	Outward Significant	Outward Significant	Destruction Significant	Destruction Limited	High
0.1134 kg/s	Outward Significant	Outward Significant	Destruction Significant	Destruction Limited	High
0.1589 kg/s	Outward Significant	Outward Significant	Outward Significant	Destruction Limited	High
0.2268 kg/s	Inward Significant	Outward Significant	Outward Significant	Destruction Limited	Low
0.4536 kg/s	Inward Limited	Inward Limited	Inward Limited	Outward Limited	Low
Influence	High	High	High	Low	

The purpose is to provide a reference for rapidly evaluating the impacts of these two parameters in the design of jet-based systems, thereby reducing the workload of conceptual design engineers. For example, as can be seen from the table, the drag reduction effect is optimal and less susceptible to freestream angle-of-attack interference when the mass flow rate is 0.2268 kg/s. Therefore, to achieve the optimal drag reduction performance in engineering practice, further exploration can be conducted to identify the appropriate mass flow rate in the vicinity of 0.2268 kg/s.

5. Conclusions

The study aimed to examine the effect of the counterflowing jet on the aerodynamic properties and its surrounding flow structure of the Apollo return capsule during re-entry. Numerical investigations were conducted under a series of mass flow rates and freestream angles of attack conditions. The main conclusions are as follows:

(1) As the angle of attack increases, the structure of the flow field in the LPM is readily destroyed. In contrast, the structure of the flow field in the SPM is more stable, and there are two types of inward and outward offsets of the detached bow shock and Mach disk on the windward side, which are influenced by the nozzle mass flow rate and the angle of attack. The former phenomenon occurs as the windward side of the Mach disk is subjected to greater squeeze by the freestream, resulting in the Mach disk moving inwards and transforming into a stronger normal shock. This induces the inward movement of the detached bow shock. The latter situation arises because the windward side of the recirculation region undergoes more squeezing, causing the Mach disk to move outwards and turn into an oblique shock. This leads to the outward movement of the detached bow shock.

(2) Within the limited angle of attack, the counterflowing jet under the SPM can significantly reduce the drag of the re-entry capsule. The drag reduction effect is weakened or even disappears as the angle of attack increases. For the 2.6% subscale model of the Apollo capsule investigated in this paper, it has been demonstrated that a drag reduction of approximately 50% can be achieved by the counterflowing jet with a nozzle mass flow of 0.1134 kg/s when the angle of attack is within 10°.

Overall, this research offers aerodynamic data and flow structure analyses for the re-entry process of the Apollo return capsule. It also summarizes the laws governing the influence of mass flow rates and freestream angles of attack on the interference characteristics of the counterflowing jet.

Author Contributions: Conceptualization, Z.-K.L. and L.-F.L.; methodology, S.-S.L. and Y.-L.L.; software, S.-S.L. and L.-F.L.; validation, Y.-L.L.; formal analysis, Z.-K.L.; investigation, Z.-K.L.; resources, S.-S.L.; data curation, Z.-K.L.; writing—original draft preparation, Z.-K.L.; writing—review and editing, S.-S.L.; visualization, Y.-L.L.; supervision, L.-F.L.; project administration, Z.-K.L.; funding acquisition, S.-S.L. All authors have read and agreed to the published version of the manuscript.

Funding: This research was funded by the National Numerical Windtunnel project of China (NNW).

Institutional Review Board Statement: Not applicable.

Informed Consent Statement: Not applicable.

Data Availability Statement: The data supporting the findings of this study are available in this paper.

Conflicts of Interest: The authors declare no conflicts of interest.

Abbreviations

The following abbreviations are used in this manuscript:

Nomenclature

X	X-coordinate direction
Y	Y-coordinate direction
Z	Z-coordinate direction
A	area of nozzle inlet
d	body diameter
D_0	total drag force without jet
D_{in}	drag force on the inner wall surface of nozzle
D_j	total drag force with jet
D_{out}	aerodynamic drag
ΔD	rate of change in drag force
F_T	jet reaction thrust
ID	case identifier
L_d	diameter of nozzle exit
L_j	length of Mach disk
L_r	length of recirculation region boundary
$\dot{m}_j$	mass flow rate of nozzle
M_j	nozzle exit Mach number
M_∞	freestream Mach number
P	static pressure
P_0	stagnation pressure
Re_∞	freestream Reynolds number
S_d	distance from nozzle exit to maximum cross-section
S_j	distance between Mach disk and nozzle exit
T	static temperature
T_0	stagnation temperature
α	angle of attack
β	angle of recirculation region lateral boundary
γ_∞	freestream specific heat ratio
γ_j	jet specific heat ratio
θ	angle of jet boundary

Abbreviations

CFD	computational fluid dynamics
LPM	long penetration mode
SPM	short penetration mode
DPLUR	data-parallel lower-upper relaxation
RANS	Reynolds-averaged Navier–Stokes
SST	shear stress transport

References

1. Raj, C.A.S.; Narasimhavaradhan, M.; Vaishnavi, N.; Arunvinthan, S.; AL Arjani, A.; Pillai, S.N. Aerodynamics of ducted re-entry vehicles. *Chin. J. Aeronaut.* **2020**, *33*, 1837–1849. [CrossRef]
2. Khan, S.B.; Maqsood, A.; Akhtar, S.; Xie, D.; Riaz, R. Causation of Supersonic Limit Cycle Oscillations in Atmospheric Entry Vehicles. *AIAA J.* **2022**, *59*, 960–974.
3. Ahmed, M.Y.M.; Qin, N. Forebody shock control devices for drag and aero-heating reduction: A comprehensive survey with a practical perspective. *Prog. Aerosp. Sci.* **2020**, *112*, 100585. [CrossRef]
4. Placco, L.; Cogo, M.; Bernardini, M.; Aboudan, A.; Ferri, F.; Picano, F. Large-Eddy Simulation of the unsteady supersonic flow around a Mars entry capsule at different angles of attack. *Aerosp. Sci. Technol.* **2023**, *143*, 108709. [CrossRef]
5. Pollock, R.D.; Hodkinson, P.D.; Smith, T.G. Oh G: The x, y and z of human physiological responses to acceleration. *Exp. Physiol.* **2021**, *106*, 2367–2384. [CrossRef]

6. Zhu, L.; Li, W.; Tian, X.; Song, J.; Hu, B. Establishment process of spiked lateral jet in hypersonic flows. *Aerosp. Sci. Technol.* **2022**, *124*, 107507. [CrossRef]
7. Su, Y.; Sun, P.; Cui, Y.; LE, G. Re-entry rocket basic flow characteristics and thermal environment of different retro-propulsion modes. *Chin. J. Aeronaut.* **2024**, *37*, 190–203. [CrossRef]
8. Liu, S.; Yan, C.; Kang, D.; Jiang, Z.; Sun, M. Opposing jets for heat flux reduction and uncertainty analysis on a V-shaped blunt leading edge. *Aerosp. Sci. Technol.* **2023**, *138*, 108353. [CrossRef]
9. Farr, R.; Chang, C.-L.; Jones, J.H.; Dougherty, N.S. On the Comparison of the Long Penetration Mode (LPM) Supersonic Counterflowing Jet to the Supersonic Screech Jet. In Proceedings of the 21st AIAA/CEAS Aeroacoustics Conference, Dallas, TX, USA, 22–26 June 2015; p. 3126.
10. Fan, B.; Huang, J. Coupled Fluid-Thermal Investigation on Drag and Heat Reduction of a Hypersonic Spiked Blunt Body with an Aerodisk. *Aerospace* **2022**, *9*, 19. [CrossRef]
11. Xie, Z.; Liu, C.; Meng, Y.; Huang, W.; Liang, Y.; Zhao, Z. Drag reduction mechanism based on the aerospike-jet composite approach under different incoming dynamic pressures. *Acta Astronaut.* **2024**, *225*, 741–757. [CrossRef]
12. Chang, C.-L.; Venkatachari, B.S.; Cheng, G. Effect of Counterflow Jet on a Supersonic Reentry Capsule. In Proceedings of the 42nd AIAA/ASME/SAE/ASEE Joint Propulsion Conference & Exhibit, Sacramento, CA, USA, 9–12 July 2006; p. 4776.
13. Zhang, W.; Wang, X.; Zhang, Z.; Su, T. Numerical Investigation on the Jet Characteristics and the Heat and Drag Reductions of Opposing Jet in Hypersonic Nonequilibrium Flows. *Aerospace* **2022**, *9*, 554. [CrossRef]
14. Zhang, W.; Wang, S.; Wang, Q.; Ju, S.; Yan, C. Reverse jet parameters study on aerodynamic thermal uncertainty of a blunt body. *Aerosp. Sci. Technol.* **2020**, *107*, 106260. [CrossRef]
15. Zhang, X.; Dong, H.; Cao, X.; Zhou, Y.; Xie, W.; Song, W.; Wang, Y. Investigation into Shock Control and Drag Reduction Characteristics of Opposing Plasma Synthetic Jet in Mach 8 Flow. *Aerospace* **2024**, *12*, 17. [CrossRef]
16. Venkatachari, B.S.; Ito, Y.; Cheng, G.; Chang, C.-L. Numerical Investigation of the Interaction of Counterflowing Jets and Supersonic Capsule Flows. In Proceedings of the 42nd AIAA Thermophysics Conference, Honolulu, HI, USA, 27–30 June 2011; p. 4030.
17. Guo, X.; Zhou, C. Behaviors of the long penetration mode with a hot counterflowing jet. *Aerosp. Sci. Technol.* **2022**, *130*, 107941. [CrossRef]
18. Shen, B.; Liu, W.; Yin, L. Drag and heat reduction efficiency research on opposing jet in supersonic flows. *Aerosp. Sci. Technol.* **2018**, *77*, 696–703. [CrossRef]
19. Wang, Z.; Zhang, X. Parametric research on drag reduction and thermal protection of blunt-body with opposing jets of forward convergent nozzle in supersonic flows. *Acta Astronaut.* **2022**, *190*, 218–230. [CrossRef]
20. Daso, E.O.; Pritchett, V.E.; Wang, T.-S.; Ota, D.K.; Blankson, I.M.; Auslender, A.H. Dynamics of Shock Dispersion and Interactions in Supersonic Freestreams with Counterflowing Jets. *AIAA J.* **2009**, *47*, 1313–1326. [CrossRef]
21. Cheng, G.; Neroorkar, K.; Chen, Y.-S.; Wang, T.-S.; Daso, E. Numerical Study of Flow Augmented Thermal Management for Entry and Re-entry Environments. In Proceedings of the 25th AIAA Applied Aerodynamics Conference, Miami, FL, USA, 25–28 June 2007; p. 4560.
22. Shahid, H.; Maqsood, A.; Xie, D. Shock Reduction through Multiple Opposing Jets in Atmospheric Entry Vehicle. In Proceedings of the AIAA SCITECH 2023 Forum, National Harbor, MD, USA and Online, 23–27 January 2023; p. 2116.
23. Bharghava, D.S.N.; Mali, A.K.; Jana, T.; Kaushik, M. Implementation of concavity over heat shield of a reentry vehicle in reducing aerodynamic heating. *Int. J. Heat Fluid Flow* **2024**, *107*, 109413. [CrossRef]
24. Deng, F.; Xie, F.; Huang, W.; Zhang, D.; Jiao, Z.; Chen, J.; Liu, S. Applications of counterflowing jet technology in hypersonic vehicle. *Acta Aerodyn. Sin.* **2017**, *35*, 485–495.
25. Xu, H.; Li, J.; Li, X.; Ren, J. Drag and heat reduction mechanism in long and short penetration modes of opposing jet under high-speed flow. *Acta Aerodyn. Sin.* **2025**, *43*, 1–17.
26. Zhang, J.; Dai, Z.; Li, R.; Deng, L.; Liu, J.; Zhou, N. AcceleSration of a production-level unstructured grid finite volume CFD code on GPU. *Appl. Sci.* **2023**, *13*, 6193. [CrossRef]
27. Cui, P.; Li, H.; Jia, H.; Li, L.; Qin, F.; Wu, X.; Zhang, Y. An improved Harten–Lax–Leer–Einfeldt plus plus scheme for unstructured grid and cell-centred finite-volume method. *Phys. Fluids* **2025**, *37*, 076130. [CrossRef]
28. Zhao, H.; Yang, Y.; Zhang, Y.; Li, W. Simulation Research on the Effect of Reynolds Number on the Aerodynamic Characteristics of High Lift Device. *J. Phys. Conf. Ser.* **2022**, *2280*, 012010. [CrossRef]
29. Jiang, Q.F.; Chen, S.S.; Yang, H.; Zhang, Z.G.; Gao, Z.H. Unsteady aerodynamic characteristics of a morphing tail configuration. *Phys. Fluids* **2024**, *36*, 036133. [CrossRef]
30. Cui, P.; Wu, X.; Chen, J.; Jia, H.; Qin, F.; Zhang, J.; Zhang, Y.; Zhou, G.; Tang, J. A Viscous Boundary Layer Mesh Adaptation Method and Its Application in High-Angle-of-Attack Separated Flows. *Appl. Sci.* **2025**, *15*, 11615. [CrossRef]
31. Menter, F.R.J.A.J. Two-equation eddy-viscosity turbulence models for engineering applications. *AIAA J.* **1994**, *32*, 1598–1605. [CrossRef]

32. Korzun, A.M.; Cordell, C.E.C., Jr.; Braun, R.D. Computational Aerodynamic Predictions of Supersonic Retropropulsion Flowfields. *J. Spacecr. Rockets* **2013**, *50*, 950–960. [CrossRef]
33. Ried, R.C., Jr.; Rochelle, W.C.; Milhoan, J.D. Radiative Heating to the Apollo Command Module: Engineering Prediction and Flight Measurement. 1972; No. MSC-06834. Available online: https://ntrs.nasa.gov/citations/19720017314 (accessed on 1 April 1972).
34. Venkatachari, B.S.; Cheng, G.; Chang, C.-L.; Zichettello, B.; Bilyeu, D.L. Long Penetration Mode Counterflowing Jets for Supersonic Slender Configurations—A Numerical Study. In Proceedings of the 31st AIAA Applied Aerodynamics Conference, San Diego, CA, USA, 24–27 June 2013; p. 2662.
35. Chen, L.; Wang, G.; Lu, X. Numerical investigation of a jet from a blunt body opposing a supersonic flow. *J. Fluid Mech.* **2011**, *684*, 85–110. [CrossRef]
36. Lee, J.; Lee, H.J.; Huh, H. Drag reduction analysis of counterflow jets in a short penetration mode. *Aerosp. Sci. Technol.* **2020**, *106*, 106065. [CrossRef]

Disclaimer/Publisher's Note: The statements, opinions and data contained in all publications are solely those of the individual author(s) and contributor(s) and not of MDPI and/or the editor(s). MDPI and/or the editor(s) disclaim responsibility for any injury to people or property resulting from any ideas, methods, instructions or products referred to in the content.